

UNIVERSITY OF ROCHESTER

**Digital Signal Processing of Scintillator Pulses in Nuclear  
Physics Techniques**

by

**Saba Zuberi**

A THESIS SUBMITTED  
IN FULLFILLMENT OF THE  
REQUIREMENTS FOR THE

**Senior Thesis**

FACULTY SPONSOR

**Frank Wolfs, Professor  
Physics and Astronomy**

APRIL 2003

# TABLE OF CONTENTS

ABSTRACT-----	3
1. INTRODUCTION -----	4
2. PROTOTYPE DIGITAL PULSE PROCESSOR DDC-1-----	6
2.1. DIGITIZATION PROCESS-----	7
2.2. DIGITAL PROCESSING-----	9
2.3. DATA ACQUISITION -----	11
3. INTRINSIC RESOLUTION OF DDC-1-----	12
4. RESPONSE OF DDC-1 TO SCINTILLATOR PULSES-----	12
4.1. APPLICATION TO FAST PLASTIC- -----	12
4.2. APPLICATION TO NAI(TL) DETECTOR-----	14
5. DIGITAL $\gamma$ -RAY SPECTROSCOPY-----	14
6. PULSE SHAPE DISCRIMINATION AND PARTICLE IDENTIFICATION-----	16
6.1. PULSE SHAPE DEPENDENCE ON RADIATION TYPE-----	16
6.2. EXPERIMENTAL PROCEDURE FOR PARTICLE IDENTIFICATION-----	18
6.3. RESULTS-----	22
6.3.1.ALPHA- $\gamma$ PARTICLE IDENTIFICATION-----	22
6.3.2. BACKGROUND RADATION-----	26
6.3.3. NONLINEAR PID RESPONSE -----	27
7. CONCLUSION-----	29
ACKNOWLEDGEMENTS-----	32
REFERENCES-----	32

## ABSTRACT

This paper describes a series of experiments and technical developments concerning the digital signal processing (DSP) of scintillator pulses in nuclear physics applications, which have been performed using the prototype single-channel digital pulse processor DDC-1<sup>1</sup>. The processor features a sampling analog to digital converter (ADC), a field programmable gate array (FPGA), and a universal serial bus (USB) interface to the host personal computer (PC). The upper limit of the intrinsic resolution of the DDC-1 was measured to be 0.63% or better. It has been demonstrated that scintillator pulses shorter than the ADC sampling period can be reliably digitized. The algorithm to perform digital  $\gamma$ -ray spectroscopy with NaI(Tl) detectors using the DDC-1 has been developed and applied to the experimental data measured during this project. Digital pulse shape analysis has been developed to perform particle identification (PID) using detectors such as a CsI(Tl) crystal or a plastic and CsI(Tl) phoswich. Alpha-particle/ $\gamma$  -ray discrimination for energies up to 5 MeV has been successfully performed using two different algorithms applied to the same data set, which allowed for an unbiased comparison of the two PID methods. Unexpected nonlinear behavior of the PID has been observed above 5.5 MeV. Detailed analysis of the digitized waveforms was performed for these high-energy events in order to identify the cause of the observed nonlinearities. Recommendations concerning the PID algorithms and digital filtering have been formulated. In addition to the algorithm development and the experimental work, the technical developments included universal serial bus (USB) firmware and the host computer data acquisition software to enable continuous data acquisition from the DDC-1. The present results were essential during the development of the 8-channel version of the digitizer, which will be used at the Relativistic Heavy Ion Collider in Brookhaven National Laboratory.

---

<sup>1</sup> Designed by Dr. W. Skulski and provided by SkuTek Instrumentation for this project at no cost.

## 1. INTRODUCTION

Developments in digital signal processing (DSP) are at the forefront of electronic instrumentation for nuclear physics. The application of DSP to nuclear physics data acquisition permits a level of flexibility in data collection and analysis that is not afforded by standard analog techniques. Digitally sampling the entire detector pulse allows detailed information to be extracted from the pulse shape thereby providing the opportunity for novel applications, such as on-line particle identification (PID) [1, 2] and position-sensitive  $\gamma$ -ray spectroscopy [3]. DSP electronics are important in achieving the goals of the proposed Rare Isotope Accelerator (RIA) [4], a major new research facility for low energy nuclear physics.

Advances in the technology of electronic sampling techniques, especially the development of fast sampling analog to digital converters (ADC), made it possible to retain the high precision of standard analog techniques while utilizing more fully the information contained in detector pulses. It has been shown that digital sampling techniques provide equal or better particle identification (PID) than analog methods for fast charged particles [5, 6]. The use of field-programmable gate array (FPGA) devices with fast sampling ADCs provides enormous power in extracting information from digitized pulses in real time. On-board FPGAs equipped with application-specific software can perform calculations in parallel, giving them both the processing power and versatility.

Unlike classic nuclear electronics, where the functionality is hardwired during the design into the electronic boards, the functions performed by the DSP electronics are largely determined by the firmware downloaded into the data processing chips, such as the on-board FPGAs and microprocessors. The tremendous flexibility afforded by this approach comes at the price of the significant amount of work required to develop the firmware. Thus, the first issue to contend with in the course of this work was the development of the application-specific software and firmware for the single-channel prototype board DDC-1. The prototype, at the time it was delivered for this project, was equipped with only the proof-of-principle firmware that provided for event triggering and

waveform collection, but did not include data processing. The first phase of this project involved the development of the data acquisition (DAQ) software for the host computer, as well as the universal serial bus (USB) firmware for the embedded microprocessor to enable continuous waveform collection. Data acquisition and analysis algorithms were then developed to investigate the application of the pulse processor to the nuclear physics techniques of particle identification (PID) and pulse-height spectroscopy. Most of the algorithm development was done on the host PC side. The optimized algorithms can be transferred to the on-board processing firmware in the next phase of development.

Once the software development was completed, several experiments were performed in the course of this work. During the data-taking runs the digitized signal waveforms were recorded to disk. This approach takes advantage of the valuable feature of the DSP electronics discussed earlier, namely the almost complete recording of the available experimental information. This permitted different algorithms to be applied to the same data set, therefore enabling unbiased comparisons to be made between different algorithms. A practical application of the advantage offered by DSP electronics, demonstrated in this paper, is the investigation of the unexpected nonlinear behavior of PID that was observed for high-energy cosmic-ray events. The waveforms of events that exhibited unexpected behavior were selected and examined in detail. A similar investigation of this nonlinear behavior with classic electronics would be much more involved and time consuming, compared to that performed with the digital electronics.

This paper is organized as follows. In section 2 the details regarding the major analog and digital components of the DDC-1 are presented. The digitization process, the sampling theorem, and the Nyquist filtering are discussed. The digital triggering in the FPGA, the role of the USB processor, and the firmware and software developments for the present applications are outlined. The intrinsic energy resolution of the board is discussed in section 3. The ability of the board to successfully digitize a variety of scintillation detector pulses is shown in section 4. In section 5 the applicability of the board to digital  $\gamma$ -ray spectroscopy is demonstrated using a NaI(Tl) detector. The energy resolution obtained with the board is compared to that achieved with other FPGA-based

digitizers. In section 6 the PID algorithms developed for alpha-particle/ $\gamma$ -ray discrimination using a plastic and CsI(Tl) phoswich detector are presented. Different analyses have been applied to the same data set and compared. The PID achieved is compared to previous results using CsI(Tl) crystals.

Based on the results of this paper, PID algorithms and digital filtering have been proposed. Further investigations into the nonlinear PID response observed with the DDC-1 are discussed. The experience developed in the course of this work was instrumental in the development of the 8-channel version of the board, the DDC-8. Its proposed applications include the real-time triggering for the PHOBOS experiment at the Relativistic Heavy Ion Collider (RHIC) in Brookhaven [7].

The work described in this paper has been carried out in the spring of 2003. It was presented at the Spring APS meeting, April 2003, Philadelphia, PA and contributed to the material presented at the Workshop on the Experimental Equipment for RIA, March 2003, Oak Ridge, TN [8, 9].

## **2. PROTOTYPE DIGITAL PULSE PROCESSOR DDC-1**

The DDC-1 is a prototype single channel board, designed for the development of DSP electronics for physics applications. It is the first step in the design of a family of digital pulse processors. The DDC-1 is divided into separate analog and digital parts and is equipped with a 12-bit, 65 MHz sampling ADC, an FPGA where triggering is carried out, a USB processor with an 8K internal memory, and a reconstruction digital to analog converter (DAC) which is very useful for development purposes. The DAC allows the manipulated waveform to be easily viewed on an oscilloscope and compared to the signal directly from the detector. An image of the board with these major components labeled is shown in Fig. 1.

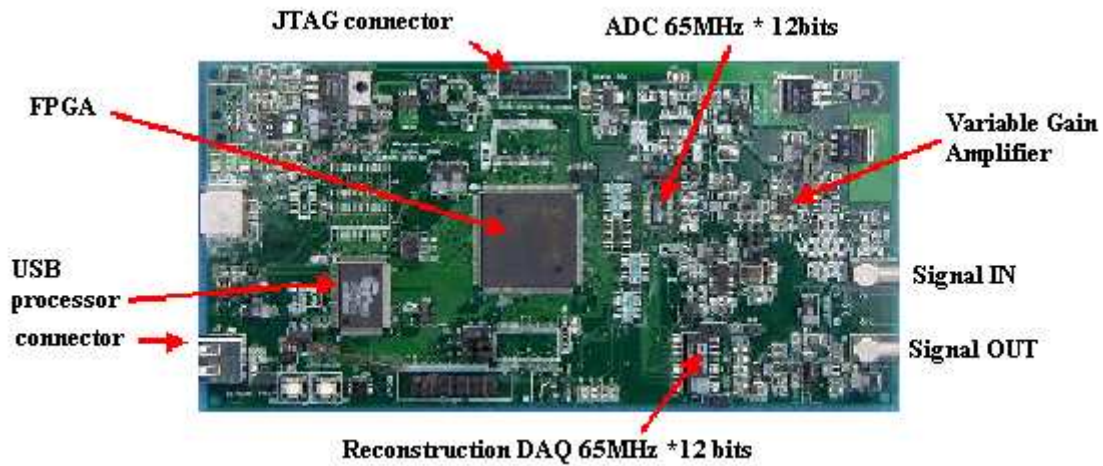


Figure 1. Image of the DDC-1 with major components labeled.

## 2.1 DIGITIZATION PROCESS

The input signal to the DDC-1 comes directly from the detector. It undergoes analog signal conditioning, such as passing through a variable gain amplifier, in order to ensure that it is within the range of the ADC. The signal passes through a low-pass analog Nyquist filter, which is the only shaping that is performed on-board and then it is sampled by the ADC. The signal-processing chain is illustrated in the block diagram of the board shown in Fig. 2.

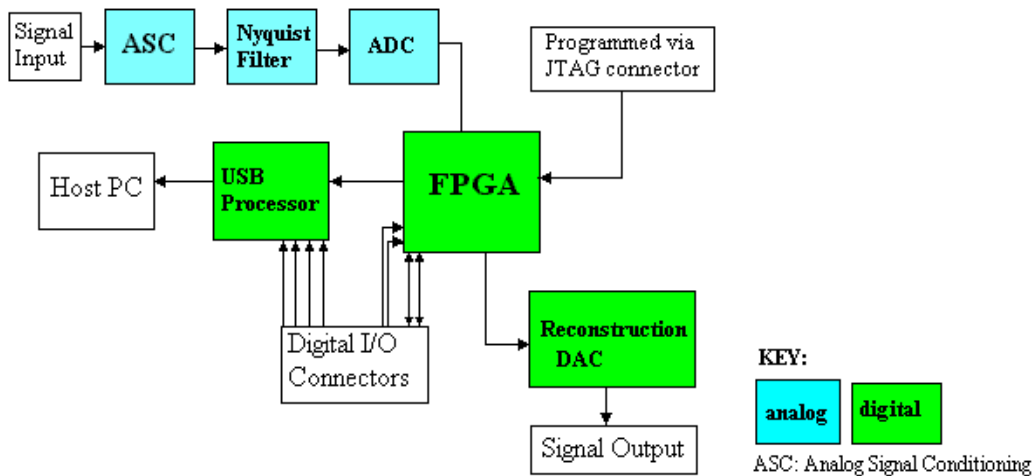


Figure 2. Block diagram of the DDC-1

Each time the incoming voltage is sampled, the ADC converts it into a 12-bit digital number. Although the ADC has a 12-bit range it spans both positive and negative voltages. All the detectors considered in this paper have unipolar signals, which leads to an effective 11-bit range of the ADC. The ADC used on the DDC-1 has another bit that is set when ADC overflow occurs, which is distinct from the 12 conversion bits.

The accuracy to which the ADC can specify the voltage signal is called the least significant bit (LSB), which is determined by the voltage range of the ADC,  $\pm 2V$  in this case, divided by the number of conversion bits. The conversion of voltage from a continuous analog value to a discrete one, quantization, corresponds to a loss of precision that adds noise to the signal. This quantization error is uniformly distributed between  $\pm LSB/2$  with

$$\sigma = \frac{LSB}{\sqrt{12}} \quad (1)$$

Therefore increasing the number of conversion bits reduces the quantization error [6].

The ADC sampling frequency,  $f_s$ , was set to 48 MHz, which is below the maximum sampling frequency of 65 MHz for this particular ADC. The information in the original signal from the detector may be completely reconstructed from the sampled waveform if and only if the ADC sampling frequency is greater than or equal to twice the highest frequency,  $W$ , of the signal. This is stated in the Nyquist-Shannon sampling theorem, “If a function  $s(t)$  has a Fourier transform  $F[s(t)] = S(f) = 0$  for  $|f| > W$ , then it is completely determined by giving the value of the function at a series of points spaced  $1/(2W)$  apart. The values  $s_n = s(n/(2W))$  are called the *samples of  $s(t)$* .”[10] Any frequency components in the input signal greater than half the sampling frequency are aliased to frequencies between DC and  $f_s/2$ , the Nyquist frequency. Such components, if present add to the noise in the digitized signal. It is therefore necessary to restrict the signal bandwidth to below  $f_s/2$ .

An analog low-pass Nyquist filter is placed before the ADC to eliminate frequencies greater than  $f_s/2$  from the signal. An ideal low-pass filter would completely suppress frequencies greater than the cut off frequency,  $f_c$ , while passing all frequencies below  $f_c$ .

completely unattenuated. Real filters exhibit a gradual drop in amplitude, called roll-off, proportional to  $f^{-N}$ , where  $N$  is the “order of the filter”. Although increasing the order of the filter yields a faster roll-off, it also increases the complexity of assembly. A compromise is required in actual instrument design. The filter used on the DDC-1 is a low-pass 3<sup>rd</sup> order Butterworth filter with a cut off frequency of 20 MHz, i.e.  $0.4f_s$ , at which the amplitude of the signal is reduced by 3dB [11].

The cut off frequency of the filter is not only important in ensuring that frequencies greater than the Nyquist frequency are suppressed, but also points to a compromise that must be made between the suppression of noise and fast pulse responses. White noise is noise in which each sample in the time domain contains no information about the other samples and has a flat frequency spectrum [12]. A lower  $f_c$  suppresses more white noise and therefore is desirable. However a lower cut off frequency corresponds to a wider filtered pulse, which makes a high  $f_c$  important for a fast pulse response.

The Nyquist filter used on the DDC-1 is the so-called Butterworth filter, which has the fastest roll-off in the frequency domain among other common filters, while still keeping the passband as flat as possible [12]. However in the time domain the impulse response of the Butterworth filter is not optimum. It shows an overshoot of about 5%, which we expect to see in the digitization of fast scintillator pulses. Since the information we are interested in is in the pulse shape, a filter that preserves the shape of the signal is desirable. As shown by Bardelli et al. [6] among the 3<sup>rd</sup> order low-pass filters the so-called Bessel filter, which minimizes the overshoot and ringing would be more appropriate even though it has poorer roll-off than the Butterworth filter.

## 2.2 DIGITAL PROCESSING

The sampled waveform passes from the ADC to the FPGA, and from there to the USB processor and also to the reconstruction DAC. These are the components in which the digital processing of the signal occurs, as indicated in Fig. 2.

The FPGA, which consists of gates, flip flops and memory elements, may be described as a “highly parallel configurable digital signal processor”. The FPGA permits

calculations to be carried out in parallel and therefore significantly increases DSP speed. The functional characteristics of the FPGA are fully determined by the “configuration file” downloaded into the chip at the run-time. The configuration is most commonly developed using the high-level language VHDL [13]. The firmware is downloaded to the FPGA via the JTAG connector (see Fig. 1, 2). The FPGA is fully reprogrammable, thereby allowing different application-specific configurations to be utilized with the same hardware.

The event trigger is either derived in real time in the FPGA or it can be obtained externally. There are four I/O connectors with lines to the FPGA (see Fig. 2) that can be used as external trigger-inputs and/or trigger-outputs, however this was not used for the present applications. The role of the trigger is to recognize when an event has arrived that needs to be processed. The trigger used in the DDC-1 is a differentiating trapezoidal filter, which differentiates the incoming ADC data and smoothes the samples. It is called a trapezoidal filter because a trapezoid best describes the step response of the filter. There are two windows of length  $0.33 \mu\text{s}$  (i.e. 16 samples), separated by a gap of the same length. The samples in the windows are summed and the trigger is issued by the FPGA firmware when the difference exceeds a certain threshold. The difference in the two sums over 16 samples reduces the noise relative to a single sample and the gap reduces the sensitivity of the trigger to variations in the rise time of the signal [1]. The width of the sampling windows and the gap may be varied by altering the firmware downloaded into the FPGA.

The trigger implemented on the DDC-1 was designed to recognize the arrival of steps in the incoming signal, such as those from RC-reset preamplifiers, which however were not used for this project. This firmware was used to process scintillator pulses and it has proven successful, and therefore was not modified for this work.

## 2.3 DATA ACQUISITION

The USB is a standard interface for communication between a computer and external components that has the advantage of being both inexpensive and common to most PCs. The DDC-1 has an on-board USB processor. It has an 8K internal memory and is programmed in programming language C. There are four I/O connectors with lines to the USB processor that can be used to control external devices, such as LEDs in the current application, that were very useful for development purposes.

The processor has 8 endpoints that are used to create paths for data flow with unique identifying addresses over which data can be transferred to the host PC. The pre-existing firmware for the DDC-1, at the time it was delivered for this project, transferred data from the board to the PC over a single endpoint of the USB processing chip. The transfer procedure uses a “blocking call” that can only return to the calling program when all of the data expected in the transfer is successfully obtained. On the PC side the driver software waits until the blocking call is returned. As a result if the user makes an acquisition request when all of the expected data is not yet available, the driver software waits and the PC appears hung. The USB firmware was therefore modified for this project to enable continuous data acquisition from the board without rendering the GUI unresponsive. A new end point was defined over which a request would be issued to the board in order to determine if data was available. A single byte was returned to the PC on the basis of which data could be requested by the host PC.

For this project, data acquisition (DAQ) software was developed that continuously acquires data from the DDC-1, displays sampled waveforms and extracts energy information by integration of the waveform. This information is graphically displayed in histograms. The DAQ software also allows parameters on the board, such as the threshold level of the differentiating trapezoidal trigger to be changed by the user.

### 3. INTRINSIC RESOLUTION OF DDC-1

The intrinsic resolution of the DDC-1 was measured using the ORTEC 480 pulser connected to the TENNELEC TC 248 amplifier. The pulse provided was approximately 6.25  $\mu$ s wide. The energy of the pulse was determined by integration and the resolution is defined

$$\frac{FWHM}{Centroid} * 100 \quad (2)$$

where FWHM is the full width at half maximum. The intrinsic energy resolution of the board was determined to be  $0.63 \pm 0.04$  %. On inspection with an oscilloscope the pulser did not appear to be very stable due to loose dial connections. It is expected that with a different pulser an improved resolution may be measured. The present figure was accepted as an upper limit of the board resolution for this project, because it does not limit the results obtained with the scintillation detectors used, whose intrinsic resolution is an order of magnitude larger.

### 4. RESPONSE OF DDC-1 TO SCINTILLATOR PULSES

The ability of the DDC-1 to handle a wide range of signals is demonstrated by considering scintillator pulses with decay times of 1.8 ns, obtained using a Bicorn BC-404 plastic scintillator and 0.23  $\mu$ s using a Bicorn NaI(Tl) crystal. Organic scintillators, such as plastics, are aromatic hydrocarbons where scintillation arises from the transition of free valence electrons. They exhibit much faster decay times than inorganic scintillators in which scintillation arises from transitions in an electron band structure, which is discussed further in section 6.1.

#### 4.1 APPLICATION TO FAST PLASTIC

The DDC-1 was used to collect digitized waveforms from a Hamamatsu R1450 photomultiplier tube (PMT) coupled to a 1x1x1 cm<sup>3</sup> cubic plastic BC-404 scintillator. The original pulse from the BC-404 scintillator has a decay time of 1.8 ns and has a width

of 12 ns that includes the PMT response. The output signal at the PMT is shown in Fig. 4a on a digital oscilloscope, which has much faster sampling frequency and no Nyquist filter. The ADC has a sampling rate of 48 MHz and so the incoming signal is sampled once every 20.8 ns, which is almost twice the width of the pulse from the plastic scintillator. As seen in Fig. 4b the DDC-1 successfully digitizes this very fast pulse. The analog Nyquist filter restricts the signal bandwidth from DC to 20 MHz causing the shaped signal to be spread out in time (see section 2.1). Due to the filter the waveform from the plastic has a width of approximately 63 ns as observed in Fig. 4b. Without the Nyquist filter, the digitized waveforms from the fast plastic scintillator would have at most one sample in the pulse, therefore the Nyquist filter is critical in allowing fast plastic waveforms to be digitized successfully. As expected an overshoot is seen in the digitized waveform in Fig. 4b due to the impulse response of the Butterworth filter, as discussed in section 2.1. The Bessel filter would minimize such an overshoot, which is important for the digitization of fast pulses, and has therefore been used in the 8-channel version of the digitizer.

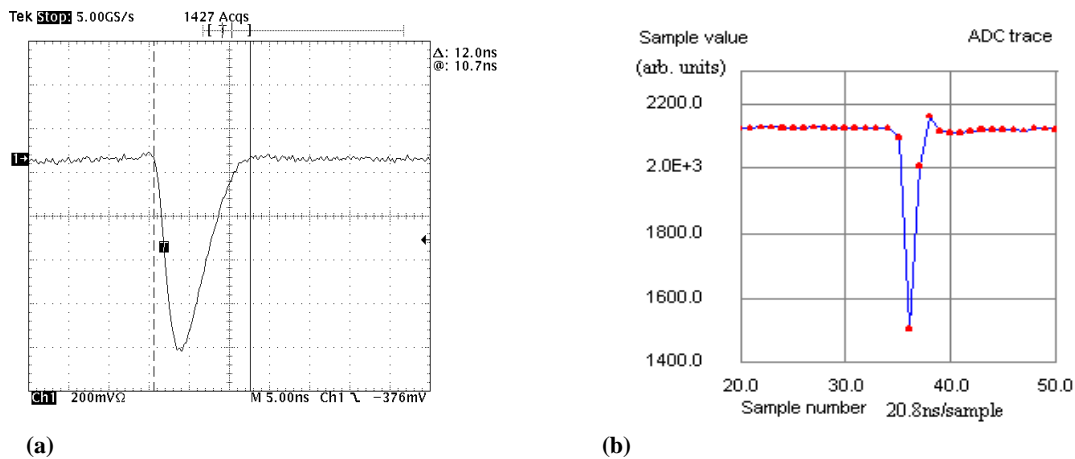


**Figure 4 (a) The signal directly from the BC-404 plastic scintillator and R1450 PMT on an oscilloscope with a width of 12ns (1 sample = 0.2 ns) (b) The digitized waveform acquired from a fast plastic scintillator (1sample=20.8ns) with the DDC-1.**

## 4.2 APPLICATION TO NAI(TL) DETECTOR

The response of the DDC-1 to a much slower pulse has also been studied. A 2"x2" cylindrical Bicorn NaI(Tl) detector, which has an effective decay time of 0.23  $\mu\text{s}$ , was used with a  $^{137}\text{Cs}$  radioactive source. The digitized waveform shown in Fig. 5 has a width of approximately 1.66  $\mu\text{s}$ , once filtered. As expected, the DDC-1 has a good response to slower pulses. In this case the original pulse is sufficiently spread in time, however the Nyquist filter is still essential in order to decrease the white noise that can be present in the signal above the filters cut off frequency.

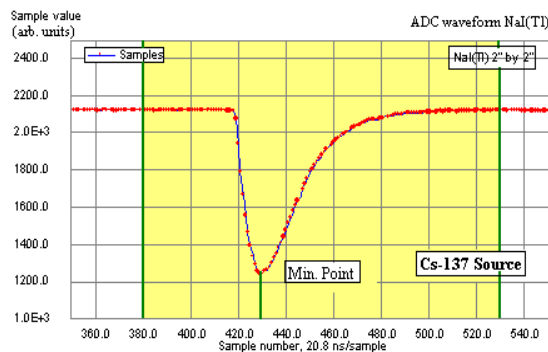


**Figure 5.** The digitized waveform acquired from a NaI(Tl) detector with  $^{137}\text{Cs}$  source, where the yellow area indicates the window used to determine energy of pulse.

## 5. DIGITAL $\gamma$ -RAY SPECTROSCOPY

The DDC-1 was used as a digital spectrometer system to conduct a  $\gamma$ -ray spectroscopy experiment. A 2"x2" cylindrical Bicorn NaI(Tl) detector, surrounded by a lead casing, was used to collect signals.  $^{137}\text{Cs}$  and  $^{60}\text{Co}$  radioactive sources were used to investigate the resolution of the DDC-1 used as a digital spectrometer. The host PC digitally integrated the pulses, using a window defined to be 1.02  $\mu\text{s}$  before and 2.08  $\mu\text{s}$  after the minimum value of the sampled waveform, as indicated in Fig. 5. The baseline was sampled 4  $\mu\text{s}$  before and after the pulse and the average base value was subtracted from the integral of the signal. The energy spectra obtained with  $^{137}\text{Cs}$  and  $^{60}\text{Co}$  are shown in Fig. 6.

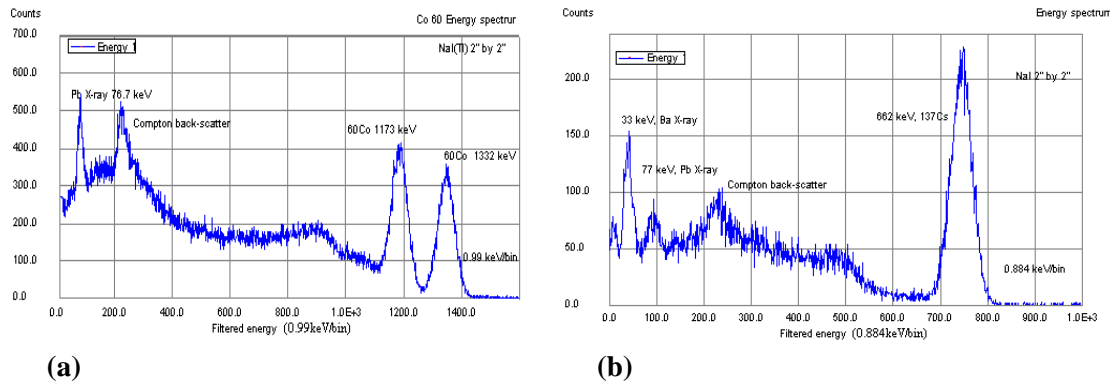


**Figure 6. Energy spectra collected with NaI(Tl) detector and a) <sup>60</sup>Co source and (b) <sup>137</sup>Cs source**

In the spectra collected from both sources an energy peak at approximately 77 keV is seen, which originates from the X-rays emitted from the lead casing around the NaI(Tl) detector. In the low energy region of the <sup>137</sup>Cs spectrum, the <sup>56</sup>Ba characteristic X-ray peak at 33 keV is measured, which has a FWHM of 23.2 keV. This however this is a composite peak and the independent K<sub>α</sub>, K<sub>β</sub> peaks have not been resolved. In the higher energy region, the FWHM of the <sup>137</sup>Cs γ–peak at 662keV is 7.1% (see Fig. 6a). The <sup>60</sup>Co γ–peak at 1173 keV has a resolution of 6.4% and at 1332 keV has a resolution of 5.2% (see Fig. 6b). Bolic and Drndarevic use an FPGA-based electronics unit with an 8 bit, 60 MHz ADC to perform γ-ray spectroscopy using a 3”x3” NaI(Tl) detector [14]. They used <sup>137</sup>Cs and <sup>60</sup>Co sources to determine the energy resolution of their system. They also reported the energy resolution obtained by classical analog spectroscopy. Their results are compared with those obtained with the DDC-1 in Table 1.

Source	DDC-1 Resolution(%)	Bolic and Drndarevic Resolution (%) [14]	Classical Spectrometer Resolution (%) [14]
<sup>137</sup> Cs	7.1	7.5	6.8
<sup>60</sup> Co	5.2	5.6	5.1

**Table 1. NaI(Tl) energy resolution for different low count rate sources measured with the DDC-1, the digitizer from [14] and a classical spectrometer from [14].**

From Table 1 we see that the energy resolution obtained with the DDC-1 is comparable to that measured by Bolic and Drndarevic both digitally and using a classical analog spectrometer. In all cases the energy resolution is limited by the NaI(Tl) crystal resolution and not by the spectrometers themselves.

The potential extension of the DDC-1 to perform  $\gamma$ -ray spectroscopy at high count rates is indicated by the ability of the similar FPGA-based digitizer used in [14] to process 400,000 counts per second. This would require the development of appropriate firmware that must include pulse pile up detection, which becomes significant at high count rates.

## **6. PULSE SHAPE DISCRIMINATION AND PARTICLE IDENTIFICATION**

### **6.1 PULSE SHAPE DEPENDENCE ON RADIATION TYPE**

The inorganic scintillator CsI(Tl) has been commonly used for pulse shape discrimination, both with traditional analog methods [15, 16] and with digital methods [5, 6, 17]. Inorganic scintillators have an electron band structure, unlike the molecular structure of organic scintillators, and have impurities added, such as Thallium in the case of CsI(Tl), which creates local energy levels in the energy gap. Ionizing radiation excites electrons in the valence band to the conduction band resulting in a free electron and a free hole; it also creates excitons, or loosely bound electron-hole pairs (see Fig. 7). These pairs move within the lattice structure and when a hole encounters an impurity atom it can be ionized attracting subsequent electrons that can then de-excite and emit radiation [18].

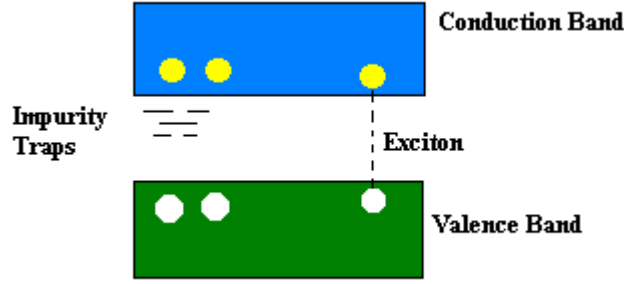


**Figure 7. Electron band structure of inorganic scintillators**

Excitons are captured as a whole by impurity atoms and the resulting radiative excited states decay faster than the single free electrons and holes, which cause the excitation of metastable states of the impurity atoms. A metastable state is one that is above the minimum energy state of the system, but requires an input of energy before it can decay to a lower energy state. Hence there are two decay components that govern the reemission of light in CsI(Tl), which may be described by

$$N(t) = A \exp\left(\frac{-t}{\tau_f}\right) + B \exp\left(\frac{-t}{\tau_s}\right) \quad (2)$$

where  $N(t)$  is the number of photons at time  $t$ , and  $\tau_f$  and  $\tau_s$  are the fast and slow decay components respectively [19].

While the fast decay components dominate the light emission of most scintillators, CsI(Tl) has a substantial slow component. The energy loss per unit path length,  $dE/dx$ , of the incident particle causes the different excited states of the scintillator to be populated differently. Consequently, the relative intensities of  $\tau_f$  and  $\tau_s$ , and the resulting pulse shape from the PMT will depend on the type of incident particle. Therefore CsI(Tl) scintillators can be used to perform particle identification (PID) based on pulse shape discrimination.

Particles with high ionization densities,  $dE/dx$ , produce relatively more excitons than particles with lower ionization densities and consequently have a smaller effective decay component. This is demonstrated in Fig. 8 where the digitized waveforms are shown from the DDC-1 and a  $1 \times 1 \times 1 \text{ cm}^3$  cubic CsI(Tl) scintillator detector with a  $^{232}\text{Th}$  source that emits alpha particles and  $\gamma$ -rays. Alpha particles have a high ionization density and

an effective decay time of  $0.425 \mu\text{s}$  in CsI(Tl), in comparison with  $\gamma$ -rays which have a low ionization density and a longer effective decay time of  $0.695 \mu\text{s}$  [19].

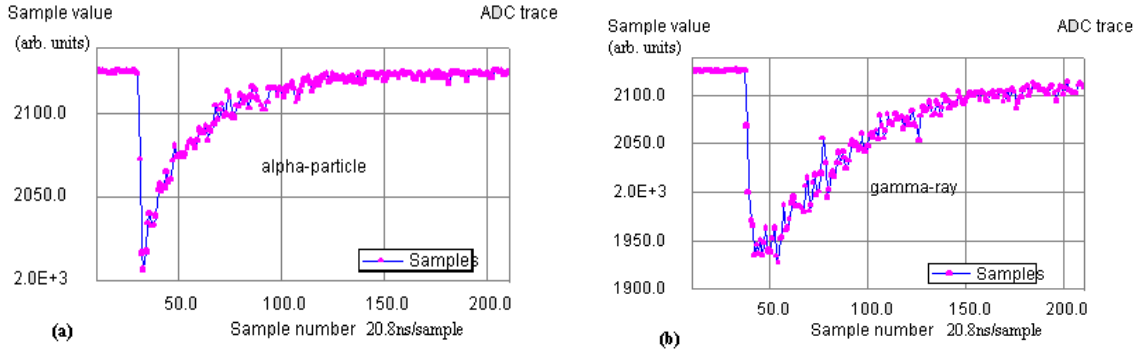


**Figure 8. Digitized waveform of an alpha-particle in a) and a  $\gamma$ -ray in b) in a CsI(Tl) detector with a  $^{232}\text{Th}$  source**

From Fig. 8 a clear pulse shape dependence of the digitized waveform on the type of radiation is seen using the DDC-1. This implies that comparing the integrals of different parts of the CsI(Tl) signal will enable discrimination between alpha particles and  $\gamma$ -rays to be performed.

## 6.2 EXPERIMENTAL PROCEDURE FOR PARTICLE IDENTIFICATION

The detector used for pulse shape discrimination is a phoswich detector, which is a  $1 \times 1 \times 1 \text{ cm}^3$  CsI(Tl) crystal coupled to a  $1 \times 1 \times 0.8 \text{ cm}^3$  Bicron BC-404 plastic scintillator and a R4214 Hamamatsu phototube (see Fig. 9a). There is a thin aluminum foil window in front of the CsI(Tl) crystal, which is not wrapped in Teflon in order to permit the penetration of alpha particles while shielding the detector from ambient light. The phoswich detector was used, rather than simply a CsI(Tl) crystal in order to investigate the time separation of the signal components from the plastic and the CsI(Tl) parts, and to develop algorithms for devices that utilize this type of signal. Examples of such devices are the Miniball [15] and the Dwarf Ball [16], in which phoswich detectors are used for particle identification up to around  $Z \approx 20$  based on pulse shape discrimination. In both of these applications the phoswich detectors are composed of a 20 mm thick CsI(Tl) crystal

coupled to a PMT, where the face of the CsI(Tl) is coated with several micrometers of plastic scintillator. Thin plastic scintillator foil was not available for this work, therefore the arrangement shown in Fig. 9a was used.

The digitized waveform obtained from the phoswich detector with no source present is shown in Fig. 9b. Cosmic rays penetrate the CsI(Tl) crystal and then the plastic scintillator. In Fig. 9 it is shown that the fast component of the signal originating from the plastic can be clearly distinguished from the exponential decay of the light from the CsI(Tl) scintillator.

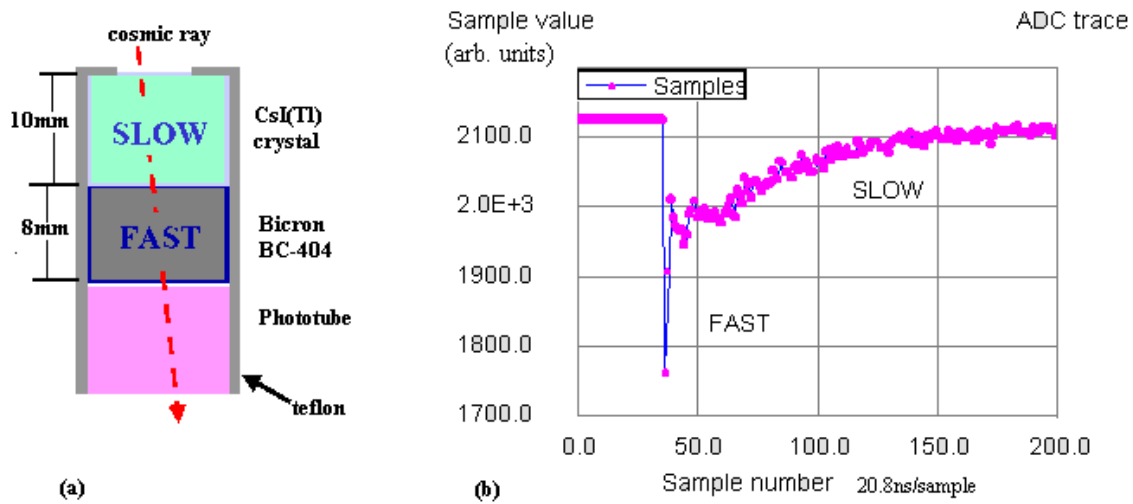


**Figure 9. a) Schematic of phoswich detector with incident cosmic ray b) Digitized waveform from cosmic ray passing through the phoswich detector.**

During the PID measurement a thick  $^{nat}\text{Th}$  source was placed 5 mm from the face of the phoswich detector. The particles emitted from the decay chain of  $^{nat}\text{Th}$  are alpha particles with energies up to 8.79 MeV and  $\gamma$ -rays with energies less than 3 MeV [16].

A leading-edge discriminator was programmed into the data acquisition software on the host PC in order to select the events to be written to disk. The threshold is set at a sample value of 2100 (see Fig. 10). The sample of the waveform that first crosses the threshold, defined on the PC side, is used to position the windows of integration of the waveform. The *fast* window is 292 ns wide, which includes 84 ns after the threshold.

The *slow* window is  $0.5 \mu\text{s}$  wide and the *tail* window is  $2 \mu\text{s}$ . In addition to these windows the *total area* of the waveform is also calculated using a window  $10.4 \mu\text{s}$  in width, which begins  $0.625 \mu\text{s}$  before the threshold. The integration window widths were chosen based on those typically used for PID with phoswich [15, 16] and CsI(Tl) detectors [17].

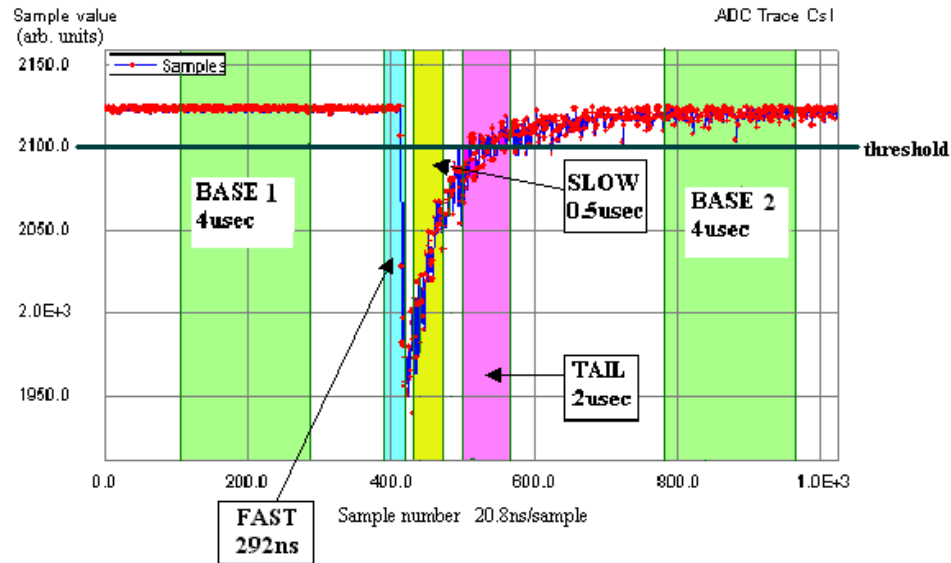


**Figure 10. Digitized waveform from phoswich and DDC-1 with overlaid windows of integration**

The baseline level is determined by averaging the value of the baseline found from windows *base\_1* and *base\_2* on either side of the pulse. This is then subtracted from the *fast*, *slow*, *tail* and *total areas*. Events where the average baseline level determined from *base\_1* and *base\_2* vary by more than 10 sample values are discarded, as either pulse pile up has occurred or the pulse did not fit within the ADC sample range. The value 10 was chosen as a generous upper bound for variations in the average values of *base\_1* and *base\_2* that are due to noise in the signal.

The clear separation of the plastic and CsI(Tl) components of the digitized signal enable waveforms that contain a predominantly plastic component to be discarded by making a cut determined by the ratio *cosmic/fast* (see Fig. 11). *Cosmic* is defined to be a 125 ns wide window in between the *fast* and *slow* windows. This cut ‘cleans’ the data

because events that are discarded, where  $cosmic/fast \leq 0.3$ , are from cosmic rays that pass predominantly through the plastic.

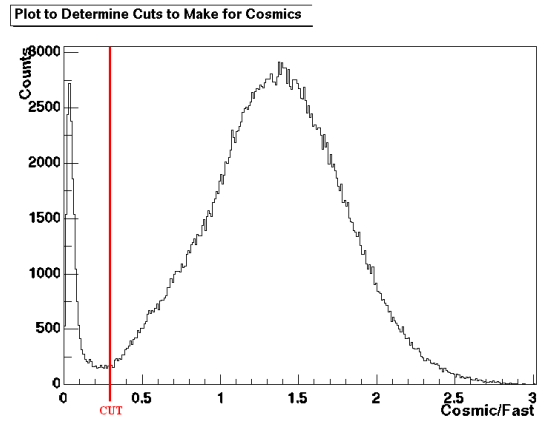
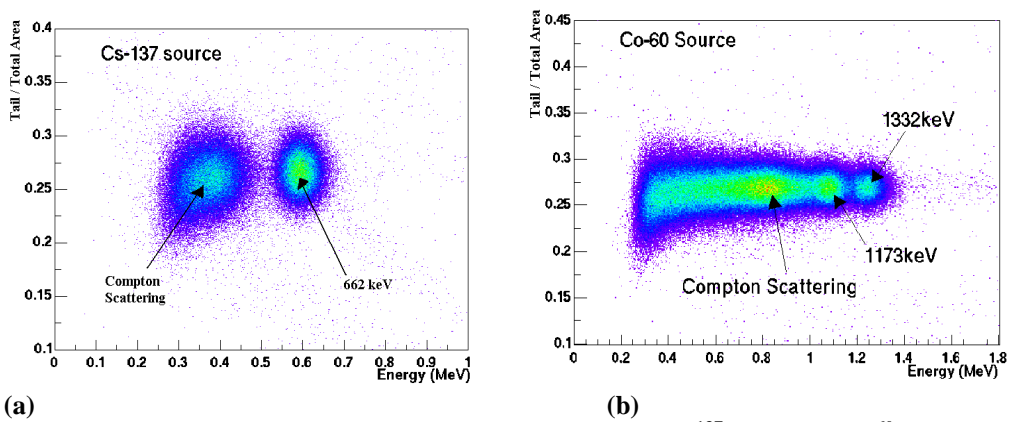


**Figure 11.** Plot to determine  $cosmic/fast$  cut to reduce cosmic ray events recorded. The events below the ‘CUT’ line are discarded.

Events where ADC overflow occurs are also discarded. This is possible since the ADC used on the DDC-1 sets a bit when ADC overflow occurs.

In order to calibrate the energy axis, the positions of the  $\gamma$ -peaks from the  $^{60}\text{Co}$  and  $^{137}\text{Cs}$  sources with the phoswich detector were used. In Fig. 12 the ratio of  $tail/total\ area$ , is plotted versus  $total\ area$  or energy. This also serves to calibrate the  $tail/total\ area$  response for  $\gamma$ -rays, which is seen to be between 0.25 and 0.29.



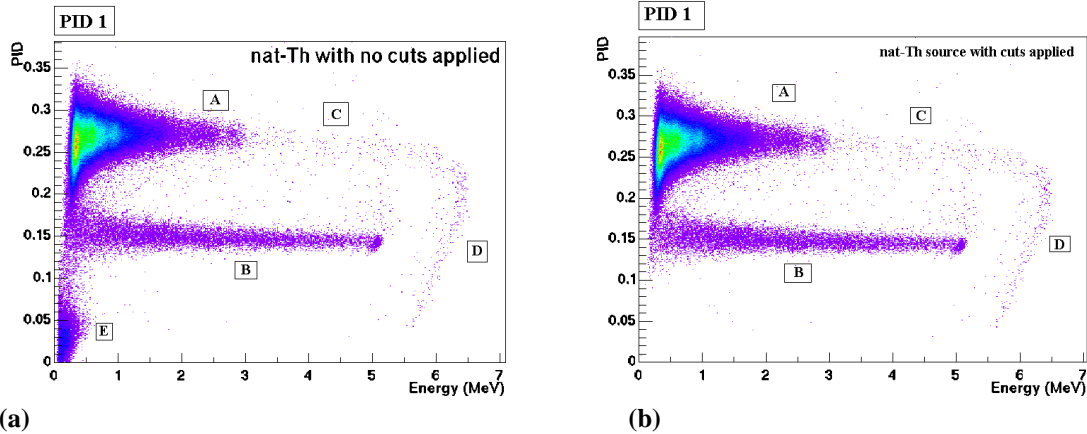
**(a)** **Figure 12.** Plot of  $tail/total\ area$  vs. Energy for a)  $^{137}\text{Cs}$  and b)  $^{60}\text{Co}$  used for energy calibration

## 6.3 RESULTS

### 6.3.1 Alpha- $\gamma$ Particle Identification

Two algorithms for performing particle identification using the  $^{nat}\text{Th}$  source and phoswich detector were implemented in this work. They were both applied to the same data set, therefore allowing an unbiased comparison to be made between them. This highlights an important advantage in data analysis that is offered by digital electronics. The two PID indexes chosen were  $PID\_1 = tail/total\ area$  and  $PID\_2 = tail/slow$ .

Fig. 13 shows the two-dimensional plots produced using  $PID\_1$  versus energy.  $PID\_1$  is seen to be independent of energy to a good approximation below 5.5 MeV, however broadens near the threshold. In Fig. 13a no cuts were applied to the data, while in Fig. 13b the cuts were applied to the same data set. This permits a reliable comparison to be made between them in order to demonstrate the effect of the cuts discussed in section 6.2. The class of events labeled ‘E’ in Fig. 13a is removed by the cut on *cosmic/fast*. These events originate from cosmic rays and/or background radiation predominantly detected in the plastic scintillator.



(a) **Figure 13.**  $^{nat}\text{Th}$  source with phoswich detector  $PID\_1$  vs. Energy (a) with no cuts applied (b) with the cuts discussed in section 6.2 applied.

Two distinct bands are obtained in the PID plots in Fig. 13. Events of classes ‘A’ and ‘C’ have a PID index of around 0.27, which is the same as that of the  $\gamma$ -peaks of  $^{60}\text{Co}$  and

$^{137}\text{Cs}$  in Fig. 12. The  $\gamma$ -rays from the decay chain of  $^{\text{nat}}\text{Th}$  are known to have energies up to approximately 3 MeV [20], which coincides with class ‘A’ events. This implies that events ‘A’ are  $\gamma$ -rays from the  $^{\text{nat}}\text{Th}$  source and that events ‘C’ are background radiation and cosmic rays with waveforms that have a significant component from CsI(Tl), unlike events ‘E’. This is further supported by the investigation of background radiation in section 6.3.2.

The events ‘B’ in Fig. 13 have a smaller  $PID\_I$  index than the  $\gamma$ -rays, suggesting that they are alpha particles. Although the decay of  $^{\text{nat}}\text{Th}$  produces alpha particles with energies up to 8.79 MeV, the source used was a thick source and the alpha particles also lose approximately 1 MeV in the 5 mm of air [21] between the source and the detector. The alpha particles are further slowed down in the aluminum foil on the surface of the phoswich. Events ‘B’ are measured to have energies up to 5 MeV, which is consistent with the energy expected for alpha particles from the source.

In order to confirm that the events in class ‘B’ are indeed alpha particles, additional data sets were collected with a piece of paper between the  $^{\text{nat}}\text{Th}$  source and the detector. The PID plot obtained is shown in Fig. 14a, where the number of events in class ‘B’ is severely diminished as compared to Fig. 13b. This implies that events ‘B’ in Fig. 13 are alpha particles.

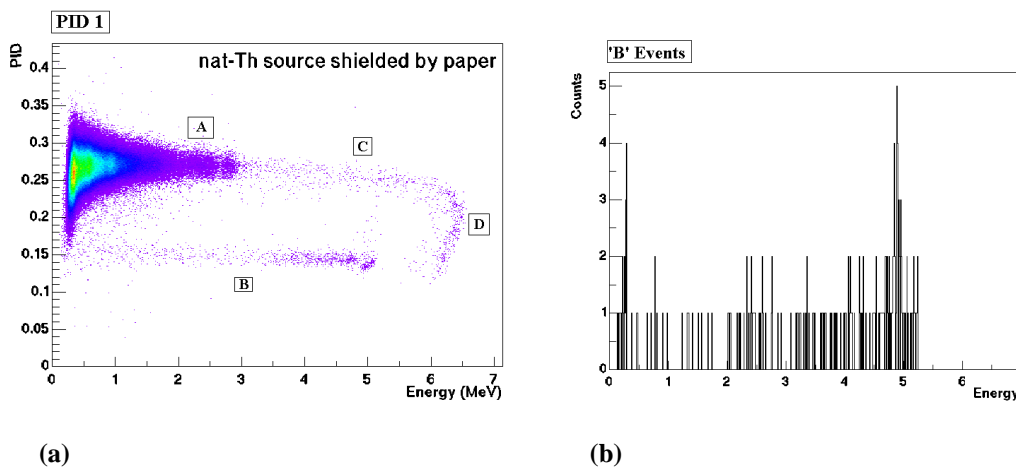


**Figure 14.**  $^{\text{nat}}\text{Th}$  source shielded by paper and phoswich detector (a)  $PID\_I$  vs. Energy with cuts applied (b) projection of ‘B’ events on energy axis.

It would be expected that all the alpha particles directly from the source would be stopped by paper. However there are still alpha particle events present, particularly with energies around 5 MeV as indicated in Fig. 14b. The measurement was repeated with a thicker cardboard shielding between the source and the detector and a similar distribution of ‘B’ events was observed. Furthermore, an investigation of background radiation (see section 6.3.2) demonstrates the presence of alpha particles with energies of approximately 5 MeV, without any source or paper present. Since these are the highest energy alpha particles measured from the source without any shielding, this suggests the possibility that there are  $^{nat}\text{Th}$  decay products, such as  $^{212}\text{Po}$ , attached to the box that houses the detector and to the face of the detector.

In addition to the identified events ‘A’, ‘B’, ‘C’ and ‘E’, there is also a class of events ‘D’ with a nonlinear PID response that are further investigated in section 6.3.3.

A similar analysis was carried out with the index  $PID\_2$  on the same data set presented in Fig. 13. The PID plot obtained is shown in Fig. 15, where the PID index is again independent of energy to good approximation below 5.5 MeV, however broadens near the threshold. Based on a similar analysis as used with  $PID\_1$ , events ‘A’ are determined to be  $\gamma$ -rays from  $^{nat}\text{Th}$ , events ‘B’ are alpha particles, and events ‘C’ are background radiation and cosmic rays with waveforms that have a significant component from CsI(Tl). An increase is seen in  $PID\_2$  for events ‘B’ at 5 MeV, which is not observed for  $PID\_1$ . Events ‘D’ again exhibit a nonlinear PID response .

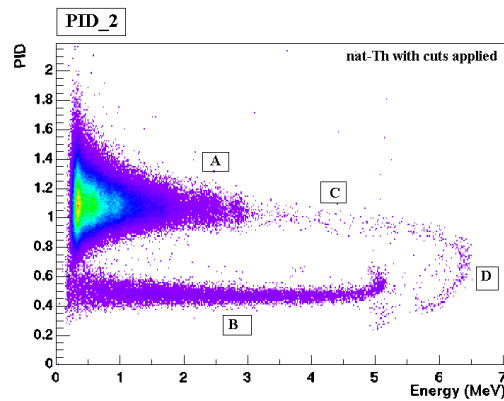


**Figure 15.**  $^{nat}\text{Th}$  source with phoswich detector  $PID\_2$  vs. Energy with cuts discussed in section 6.2 applied.

A quantitative measure of the PID capabilities of the DDC-1 with the presented algorithms is obtained from the figure of merit (FOM) of the PID index versus energy plots, which is defined as

$$FOM = \frac{\text{Separation of Centroids}}{\Sigma FWHM} \quad (3)$$

where  $FWHM$  is the full width at half maximum. A larger FOM corresponds to better particle identification, and ranges from 0 where there is no PID to greater than 2 for excellent PID [14].

PID Index	FOM	FOM
	0.5 MeV < E < 1 MeV	1 MeV < E < 4 MeV
$PID_1 = tail/total\ area$	0.92	1.75
$PID_2 = tail/slow$	1.20	1.63

**Table 2. Comparison of the FOM obtained with two different PID indexes.**

From Table 2 we see that  $PID_2$  has significantly better results at lower energies than  $PID_1$ , which has better results at higher energies. This large variation of PID with energy is demonstrated for  $PID_1$  in Fig. 16, which shows the projection on the ordinate for two energy ranges from Fig. 13b.

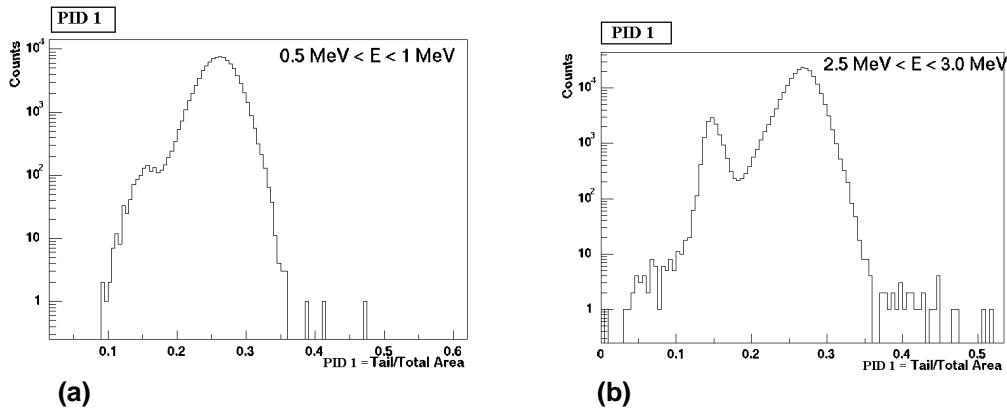


**Figure 16. Projection on ordinate from Fig. 13b for energy ranges (a) 0.5 MeV < E < 1MeV (b) 2.5 MeV < E < 3.0 MeV**

For comparative purposes we consider the results by DeVol et al. for PID with alpha particles and  $\gamma$ -rays using a computer-based digital oscilloscope and a CsI(Tl) crystal coupled to a PMT to sample the waveforms. The PID index used by DeVol et al. was *fast/tail* where the *fast* window is 0-1.1  $\mu$ s and the *tail* window 0-5.12  $\mu$ s for which a FOM of 1.4 was obtained for 0.662 MeV to 3.18 MeV [17]. The PID obtained for energy greater than 1 MeV is substantially better with the DDC-1 with both PID indexes. For CsI(Tl) with photodiode and FPGA digitizer configuration a FOM of 1.89 was obtained for energies less than 1MeV for alpha particle/ $\gamma$ -ray PID by Skulski et al., where

$$PID = \frac{\left( \frac{\sum Sample Value}{t_2 - t_1} \right)}{Pulse Height} \quad (4)$$

for  $t_1=0.5\mu$ s to  $t_2=3.25\mu$ s [5]. This is significantly better than the FOM obtained with the DDC-1 in the energy region less than 1MeV. The results discussed are summarized in Table 3.

	FOM for Energy < 1 MeV	FOM for Energy > 1 MeV
Present Work: <i>PID_1</i>	0.92	1.75
Present Work: <i>PID_2</i>	1.2	1.63
De Vol. et al. [14]	1.4	1.4
Skulski et al. [4]	1.89	-

**Table 3. Comparison of FOM achieved with different PID algorithms**

### 6.3.2 Background Radiation

The background radiation was investigated using the phoswich detector with no source present to better understand the PID plots obtained in section 6.3.1. The background plot obtained for *PID\_1* is shown in Fig. 17 with the cuts applied.

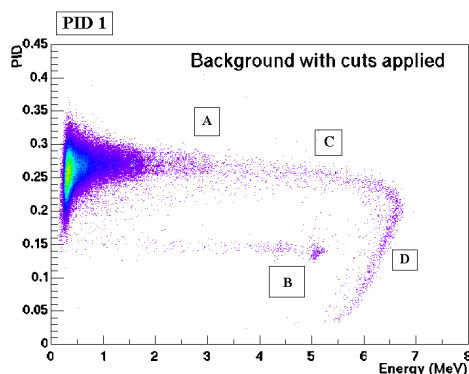


**Figure 17. Phoswich detector with no source present *PID\_1* vs. Energy with cuts applied.**

A comparison of Fig. 17 and Fig. 13b demonstrates that the class ‘D’ events occur due to background radiation. The maximum energy of ‘D’ events is approximately 6.6 MeV. This is consistent with the energy deposited by a minimum ionizing particle traveling through the full length of the phoswich detector, where  $dE/dx$  in the plastic is 1.96 MeV/cm and 5.1 MeV/cm in the CsI(Tl). This suggests that events ‘D’ are cosmic rays.

A strong similarity is seen between Fig. 17 and Fig. 14, for the  $^{nat}\text{Th}$  source shielded by paper, where alpha particles with energies of approximately 5 MeV are observed. As discussed in section 6.3.1, this supports the hypothesis that these high energy alpha particles are emanating from residual decay products of  $^{nat}\text{Th}$  on the detector and its surroundings. This may be further investigated by measuring the change in intensity of alpha ‘background’ over time to determine whether a decay time characteristic of the decay products of  $^{nat}\text{Th}$  is observed or whether a constant background alpha activity is measured.

### 6.3.3 Nonlinear PID Response

Both the PID indexes investigated show a non-linear behavior for energies between 5.5 MeV and 6.6 MeV seen in the class ‘D’ events in Fig. 13-15, 17. From section 6.2.2 it is seen that these events arise from background radiation and that their energy deposition is consistent with that expected for cosmic rays. A possible reason for this

nonlinear PID response could be due to the ADC going over range for the waveforms in ‘D’, however this possibility is excluded by the cut that is made using the ADC overflow bit. Saturation of either the PMT or in the amplifier section of the board before the ADC could potentially give rise to events ‘D’. These events could also be an effect of the CsI(Tl) and plastic detector arrangement or even a malfunction of the board.

More information may be obtained about the class ‘D’ events by looking at the pulse shape of these events. The data set from Fig. 13b was used to view the digitized waveforms of events with energy greater than 5.75 MeV. Fig. 18a shows a typical event from this high energy region with  $PID\_1$  greater than 0.25, which corresponds to events ‘C’ from Fig. 13b. While Fig. 18b shows a typical event for  $PID\_1$  less than 0.2.

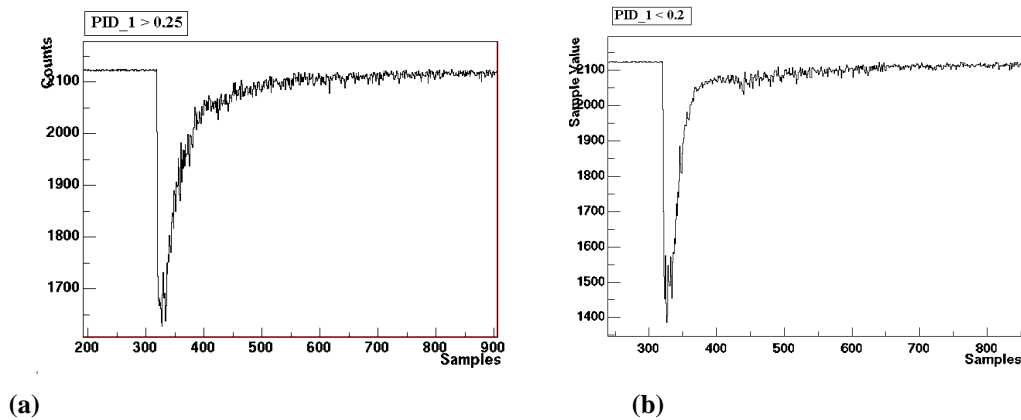


**Figure 18. Example waveform from region of Fig. 13b with  $E > 5.75 \text{ MeV}$  (a) with  $PID\_1 > 0.25$  (b) with  $PID\_1 < 0.2$**

Since the waveform in Fig. 18b is not truncated, this indicates that saturation, for example in the amplifier section of the board before the ADC is not responsible for the behavior of class ‘D’ events. No apparent malfunction in the operation of the board is seen from the waveforms of ‘D’ events, which appear to be properly digitized. There is a very striking difference between the decay components of the waveforms in Fig 18, where there is a rise in the waveform in Fig. 18b approximately  $2.4 \mu\text{s}$  after the trigger. This is consistent with the mean lifetime of a cosmic ray muon,  $(2.19703 \pm 0.00004) \mu\text{s}$

[22]. This suggests that the nonlinearities in PID observed could potentially be due to the decay of a cosmic ray muon stopped in the CsI(Tl) crystal.

## 7. CONCLUSION

The prototype FPGA-based digitizer, DDC-1, has been used in this work to develop the algorithms for digital signal processing of scintillator pulses for applications in nuclear physics. This work has provided the proof-of-principle of the ability of the DDC-1 to handle a range of scintillator pulses, and perform  $\gamma$ -ray spectroscopy and PID, demonstrating the versatility that the digital manipulation of waveforms allows. The algorithm development for spectroscopy and PID applications has been carried out on the host PC in order to refine them before committing them to the field-programmable gate array (FPGA) firmware on the DDC-1. Once the appropriate firmware has been developed, FPGA-based electronics have a major advantage over previous digitizer technology because information can be extracted from digitized waveforms in real time.

An intrinsic energy resolution of 0.63% has been measured for the DDC-1 using an ORTEC 480 pulser connected to the TENNELEC TC 248 amplifier. This places an upper limit on the resolution as fluctuations in the signal from the pulser due to loose connections may have contributed to this resolution, and a better intrinsic resolution may be measured with a different pulser.

It has been demonstrated that the DDC-1 is able to successfully digitize a wide range of scintillator pulses, including fast plastic signals with width less than half the sampling period of the ADC. The Nyquist filter used on the board, a 3<sup>rd</sup> order Butterworth filter, is critical for the digitization of fast pulses. The Butterworth filter was shown to have an overshoot in its response to fast plastic pulses in the time domain. The Bessel filter does not have an overshoot, and therefore is preferable for applications in which information is time-encoded, i.e. in the shape of the pulse. This will be the Nyquist filter used on the 8-channel digitizer extension of the DDC-1.

The applicability of the DDC-1 to digital  $\gamma$ -ray spectroscopy was demonstrated using a Bicron NaI(Tl) detector. The resolution obtained with the DDC-1 is comparable to that previously attained with an FPGA-based digitizer and analog spectroscopy techniques [14], where the energy resolution is limited by the NaI(Tl) crystal resolution and not by the DDC-1. The digitizer was able to resolve an X-ray peak as low as 33 keV, as shown in the NaI(Tl)  $\gamma$ -ray spectra for  $^{137}\text{Cs}$  (see Fig. 6a). High count rate spectroscopy will be possible with the development of appropriate firmware that would perform pile up detection.

The DDC-1 was shown to be able to carry out alpha particle/ $\gamma$ -ray identification using pulse shape discrimination. The low energy experiment was performed using a CsI(Tl) and plastic phoswich detector. A leading-edge discriminator was programmed on the host PC side and used to define the windows of integration. The plastic component of the signal was used to reduce the amount of background that was written to disk. Two PID indexes,  $PID\_1 = tail/total\ area$  and  $PID\_2 = tail/slow$ , were compared using the same data set. Energy independent PID below 5 MeV was obtained for both. The  $PID\_1$  showed better results in the region 1MeV to 4MeV, with a FOM of 1.75. However, in the 0.5 MeV to 1 MeV region  $PID\_2$  had a better FOM of 1.20. The PID algorithm could be modified to apply  $PID\_1$  in the higher energy region and  $PID\_2$  in the lower energy region. In both these regions the algorithm used gave better PID than that obtained using a CsI(Tl) and PMT configuration with a computer-based digital oscilloscope [14]. However the FOM in energy region less than 1 MeV was significantly worse than that digitally obtained with a CsI(Tl) crystal and photodiode [5]. The PID algorithm used has to be further developed to optimize the windows of integration, which will further improve the PID. The use of a digital smoothing filter is expected to also improve the PID capabilities of the DDC-1 by suppressing the high-frequency noise in the signals from the phoswich detector. In the energy region above 5.5 MeV, a variation in the  $PID\_1$  index from 0.28 to 0.04 is measured due to high energy background events. An investigation of the typical pulse shape of the waveforms in this region suggested that this behavior could be due to the decay of stopped cosmic ray muons. The multichannel

digitizer, DDC-8, could be used to perform experiments that require coincidence between scintillation detectors thereby selecting cosmic ray events for further investigation into the nonlinear PID response observed.

## ACKNOWLEDGEMENTS

I wish to thank Professor Frank Wolfs and Dr. Wojtek Skulski for their instruction and guidance. I would also like to thank Eric Johnson and Nazim Khan for their help. Finally I would like to thank Professor Bigelow for the loan of the NaI(Tl) detector used in this work.

## REFERENCES

- [1] W. Skulski et al., Act Physica Polonica B31 (2000) 47.
- [2] G.F. Knoll, Radiation Detection and Measurement, 3<sup>rd</sup> Edition, Wiley, New York, 1999.
- [3] K. Vetter et al., Nucl. Instr. and Meth. A 452 (2002) 105.
- [4] RIA, <http://www.orau.org/ria/>
- [5] W. Skulski and M. Momayezi, Nucl. Instr. and Meth. A 458 (2001) 759.
- [6] L. Bardelli et al., Nucl. Instr. and Meth. A 491 (2002) 244.
- [7] PHOBOS Detector at RHIC, <http://www.phobos.bnl.gov>
- [8] S. Zuberi, W. Skulski, F. Wolfs, *Digital Signal Processing of Fast Scintillator Pulses*, Spring APS meeting, April 2003, Philadelphia, PA.
- [9] W. Skulski, F. Wolfs, *Rochester DPP project*, RIA Workshop on the Experimental Equipment for RIA, March 2003, Oak Ridge, TN. [www.orau.org/ria/detector-03](http://www.orau.org/ria/detector-03)
- [10] [http://www.wikipedia.org/wiki/Nyquist%27s\\_theorem](http://www.wikipedia.org/wiki/Nyquist%27s_theorem)
- [11] D. Lancaster, Active Filter Cookbook, 2<sup>nd</sup> Edition, Synergetics Press, USA, 1995.
- [12] S.W. Smith, The Scientist and Engineer's Guide to Digital Signal Processing, 2<sup>nd</sup> Edition, California Technical Publishing, San Diego, 1998.
- [13] K. Skahill, VHDL for Programmable Logic, Addison Wesley Longman, Inc., CA, 1996.
- [14] M. Bolic and V. Drndarevic, Nucl. Instr. and Meth. A 482 (2002) 761.
- [15] R.T. DeSouza et al., Nucl. Instr. and Meth. A 295 (1990) 109.
- [16] D.W. Stracener et al., Nucl. Instr. and Meth. A 294 (1990) 485.
- [17] T.A. DeVol et al., Nucl. Instr. and Meth. A 435 (1999) 433.
- [18] K. Kleinknecht, Detectors for Particle Radiation, 2<sup>nd</sup> Edition, Cambridge University Press, Cambridge, UK, 1998.
- [19] W.R. Leo, Techniques for Nuclear and Particle Physics Experiments, Springer, Berlin, 1987.
- [20] C.M. Lederer et al., Table of Isotopes, Sixth Edition, John Wiley & Sons, Inc., 1967.
- [21] N. Tsoulfanidis, Measurement and Detection of Radiation, Hemisphere Publishing Corp., 1983.
- [22] Particle Data Group, Particle Physics Booklet, AIP, July 1996.